Three-dimensional xenon dendrites: Characterization of sidebranch growth

O. Wittwer* and J. H. Bilgram
Laboratorium für Festkörperphysik, ETH Zurich, CH-8093 Zurich, Switzerland
(Received 29 May 2006; published 23 October 2006)

In our experiments, we investigate *in situ* the growth of three-dimensional xenon crystals into an undercooled pure melt. Experimental studies have been extended from undisturbed growth conditions to more realistic growth conditions. Methods to characterize the transient growth of sidebranches of dendrites have been developed. Two types of sidebranches have been identified: Sidebranches initiated by selective amplification of thermal noise (type *N*) and sidebranches induced by macroscopic perturbations (type *P*). Type *N* sidebranches start to grow 3–7 tip radii behind the tip and are not correlated at the four fins. It has been verified that the sidebranch amplitude grows exponentially to $z^{2/5}$ as predicted by Brener and Temkin [E. Brener and D. Temkin, Phys. Rev. E **51**, 351 (1995)]. Type *P* sidebranches are initiated by macroscopic perturbations. They start to grow at the tip and their amplitudes are significantly higher than the ones of type *N* sidebranches. The growth of type *P* sidebranches is symmetric at the four fins. The tip positions of type *P* sidebranches separate from the tip shape of a dendrite at a distance of about $5R$ from the tip, while for type *N* sidebranches this distance is about $10R$.

DOI: 10.1103/PhysRevE.74.041604 PACS number(s): 68.70.+w, 64.70.Dv, 81.10.Fq

I. INTRODUCTION

Pattern formation is a complex process with some technological importance. Almost all alloys solidify dendritically. The solid is composed of tiny dendritic crystals stuck together. The microscopic structures formed during solidification strongly influence mechanical, chemical, and electrical properties (toughness, brittleness, electrical conductivity, corrosion behavior, etc.) of the final product. The understanding of solidification of metals is therefore of great technological and practical importance, as well as of fundamental interest for all fields where pattern formation from metastable phases at nonequilibrium conditions is studied.

Solidification is a first order phase transition where latent heat is set free at the solid-liquid interface. The initial temperature T_∞ of the melt at the beginning of growth is below the thermodynamic equilibrium melting temperature T_m. The undercooling ΔT is defined by $\Delta T \equiv T_m - T_\infty > 0$. In dimensionless units it is given by $\Delta \equiv \Delta T/(L/c_{p,l})$, with L the latent heat and $c_{p,l}$ the specific heat of the melt per unit volume. During solidification the temperature of the melt close to the surface of the crystal is near T_m, while farther away from the crystal the temperature is still at the initial temperature T_∞. The growth rate of the solidification process is governed by (i) the transport of heat and atoms from or to the solid-liquid interface by diffusion and convection, and (ii) by interfacial properties such as the solid-liquid interfacial free energy, the surface stiffness and surface kinetics, as well as their anisotropies. The physical framework of dendritic solidification is given in Sec. II.

Most metallic materials used in industrial applications are alloys where constitutional undercooling leads to an unstable solid-liquid interface during solidification. Reproducible conditions are easier to establish for pure materials where thermal undercooling is the only control parameter. Therefore we study crystal growth into a pure undercooled melt. The basis of any experimental study of solidification must be the *in situ* acquisition of 3D geometrical parameters and their development with time. Seminal experiments have been performed by the team of Glicksman. For publications in close connection with our experiments see Refs. [1–3]. Experiments with synchrotron radiation provide data out of small volumina and from quasi-two-dimensional (2D) samples only. We use xenon as a model substance for metals. Similar to metals, rare gases have a low melting entropy and according to Jackson's rule both form rough solid-liquid interfaces at atomic scale [4]. Xenon forms a simple liquid, it is chemically inert, and crystallizes in a fcc structure. Xenon is transparent and therefore we use optical imaging techniques for *in situ* observations of growing crystals. Physical properties of xenon can be found in Ref. [5]. The experimental setup is presented in Sec. III. The methods developed for a quantitative analysis of the experimental data are described in Sec. IV.

Dendrites are one of the most frequently observed shapes formed during solidification in nature. The word dendrite derives from the Greek word "dendron," meaning "tree" or "branch." Dendrites are treelike structures with a pronounced orientational order (Fig. 1). The smooth main tip of most metal and rare gas crystals grows parallel to ⟨100⟩ direction [6]. Along the growing crystal four fins develop and their amplitudes increase with distance from the tip, thus leading to the typical fourfold symmetry of the cross section of a xenon dendrite. The contour of the tip can be described by

$$z = a|x|^{5/3}, \tag{1}$$

where the crystal grows along the z direction. x and z are scaled by the radius of curvature R of the dendrite tip (tip radius), which is the typical length scale of a dendrite. Singer proposed a generalized method to measure the tip radius [7]. In the following all lengths are scaled by R.

At the distance of a few R behind the tip the fins become unstable upon thermal fluctuations and small tips begin to

*Electronic address: owittwer@solid.phys.ethz.ch

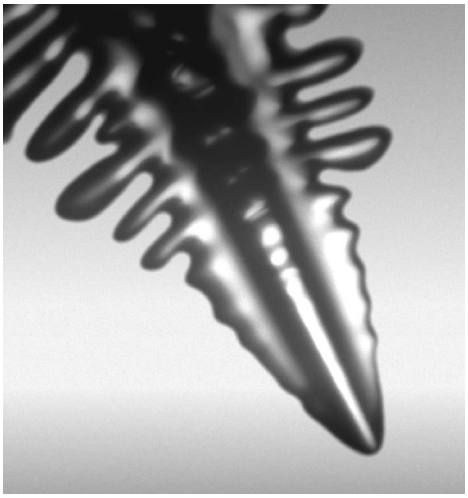

FIG. 1. A typical xenon dendrite with a pronounced orientational order and the typical fourfold symmetry at the tip region.

grow at the ridges of the fins. Further away from the dendrite tip, small sidebranch tips develop to individual sidebranches. Since the melting temperature of a convex and/or concave surface is lower and/or higher than the equilibrium melting temperature of a plane interface (Gibbs-Thomson effect [4]), a heat flow between differently curved regions is induced, leading to the growth of big sidebranches on the expense of small ones, a process which is called coarsening (Fig. 2). Larger sidebranches "survive" while the growth of smaller sidebranches is suppressed. Sidebranches are called active if they are not suppressed by other sidebranches during the time of observation. With increasing size active sidebranches develop to dendrites with a next generation of sidebranches, leading to the typical treelike structure (Fig. 1). Several phenomenological relationships between tip radius, length of the contour, and projection area have been found for stationary growing dendrites [5,7–10].

In most studies up to now where dendritic growth was studied in a stationary state, selective amplification of thermal noise is found to be the origin of sidebranching. Bisang and Bilgram [11,12] found quantitative agreement between the measured sidebranch amplitude of xenon dendrites and

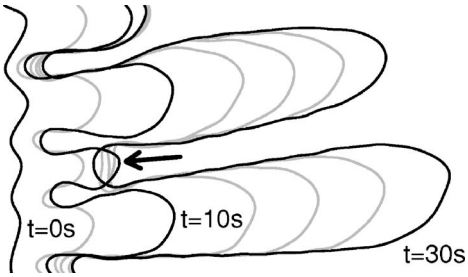

FIG. 2. Coarsening in dendritic growth. Contours of growing sidebranches at selected times. At the beginning ($t=0$ s), small sidebranches have developed at the ridge of a dendrite fin. At 10 s later the growth of the middle tip (indicated by the arrow) is suppressed by its nearest neighbors. After another 20 s the small tip has completely been "eaten up" by remelting. Also the gaps between the sidebranches have been filled up.

the analytical predictions for a nonaxisymmetric needle crystal [13]. It has been demonstrated by Singer [14] that the cross section of xenon dendrites is crosslike whereas the crosssection of SCN dendrites can be approximated much better by an axisymmetric Ivantsov dendrite. In addition to these noise induced sidebranches (type *N*), also other types of sidebranches have been observed in experiments. In quasi-2D experiments [15] localized heat pulses were applied to succinonitrile dendrite tips during directional solidification experiments. These perturbations led to sidebranches growing closer to the tip than the noise-generated sidebranches. Also convective flow can significantly influence the amplitude of sidebranches. The initiation of dominant sidebranches by pressure changes has been reported in Ref. [16]. All these sidebranches have in common that they were induced by macroscopic perturbations. Therefore we will call them "type *P*" sidebranches. In this work we report on methods that allow for a quantitative description of sidebranches. In Sec. V A the onset and amplitude of sidebranches of xenon dendrites will be discussed: The amplitudes of type *N* sidebranches as a function of distance z behind the tip will be compared to the analytical predictions in Sec. V A 1. In Sec. V A 2 the effect of macroscopic perturbations leading to type *P* sidebranches is investigated. The characteristics of active type *N* and type *P* sidebranches will be analyzed in Sec. V B according to their tip positions at larger distances behind the dendrite tip. A characterization of the envelope of a dendrite will be given in Sec. V C.

II. PHYSICAL FRAMEWORK

For a quantitative description of the dendrite problem the following assumptions are made:

(1) The crystal grows into an *infinitely large environment* of undercooled melt. Therefore no other boundaries apart from the solid-liquid interface are of importance. This growth geometry is called *free growth*.

(2) At the beginning of the experiment the entire volume of the melt is at a *homogeneous initial temperature* T_∞ below the equilibrium melting temperature $T_\infty < T_m$.

(3) The thermal diffusivities of the liquid and the solid are the same, $D_{\mathrm{th},l}=D_{\mathrm{th},s}=D$ (symmetrical model).

The propagation of a solid-liquid interface is described by the classical Stefan problem [17]. The interface is assumed to be close to the thermodynamic equilibrium melting temperature T_m. Latent heat is set free at the interface. Heat transport is described by the diffusion equation

$$\frac{\partial u}{\partial t} = D\nabla^2 u, \tag{2}$$

where u is the dimensionless thermal diffusion field around the crystal proportional to the deviation from the initial temperature,

$$u = \frac{T - T_\infty}{L/c_{p,l}} \tag{3}$$

with the local temperature T.

The energy conservation condition at the moving interface leads to the continuity equation

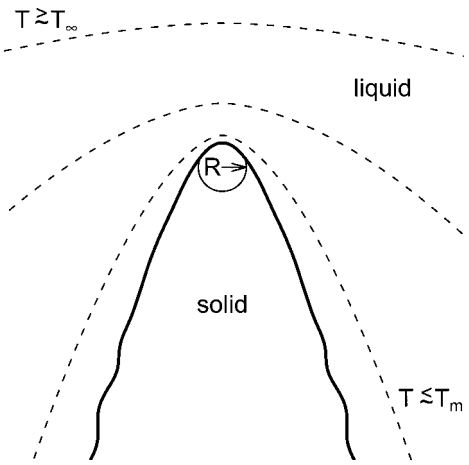

FIG. 3. Isotherms around a dendrite tip. The thermal gradient in the melt is highest at the dendrite tip and it decreases with increasing distance from the tip. Sidebranches initiated close to the tip grow faster than sidebranches initiated some distance behind the tip.

$$v_n = D(\nabla u|_{\text{solid}} - \nabla u|_{\text{liquid}}) \cdot \hat{\mathbf{n}}, \tag{4}$$

where $\hat{\mathbf{n}}$ is the unit vector normal to the interface directing into the liquid, and $v_n = \mathbf{v} \cdot \hat{\mathbf{n}}$ is the component of the growth velocity normal to the interface.

At a curved growing interface the melting temperature deviates from the thermodynamic equilibrium melting temperature. Thus the generalized Stefan problem can be written as

$$u|_{\text{interface}} = \Delta - \beta v_n - d\kappa, \tag{5}$$

where βv_n represents the kinetic effect which relates the growth velocity to the undercooling at the interface, with β the kinetic coefficient. The Gibbs-Thomson effect [4] contributes to the term $d\kappa$. For a convex surface the local curvature κ is positive. Both the capillary length d and the kinetic coefficient β can be anisotropic. For materials crystallizing in a cubic symmetry (fcc), the surface tension is assumed to have a fourfold symmetry. In this case the capillary length can be written as

$$d = d(\Theta) = d_0[1 - \epsilon_4 \cos(4\Theta)], \tag{6}$$

where ε_4 is the anisotropy strength and Θ the angle between the interface normal and a given crystallographic direction. The capillarity or average of the capillary length d_0 is a material property and is defined as

$$d_0 = \frac{\gamma_{\text{sl}} T_m c_{p,l}}{L^2}, \tag{7}$$

where γ_{sl} is the isotropic part of the interfacial free energy. d_0 is typically of the order Å.

The temperature distribution around a dendrite tip is given in Fig. 3 schematically. The dashed lines indicate the isotherms. The thermal gradient in the melt is highest at the dendrite tip and it decreases with increasing distance from the tip. Close to the dendrite interface the temperature is near the melting temperature T_m, while far away it is close to the initial temperature T_∞.

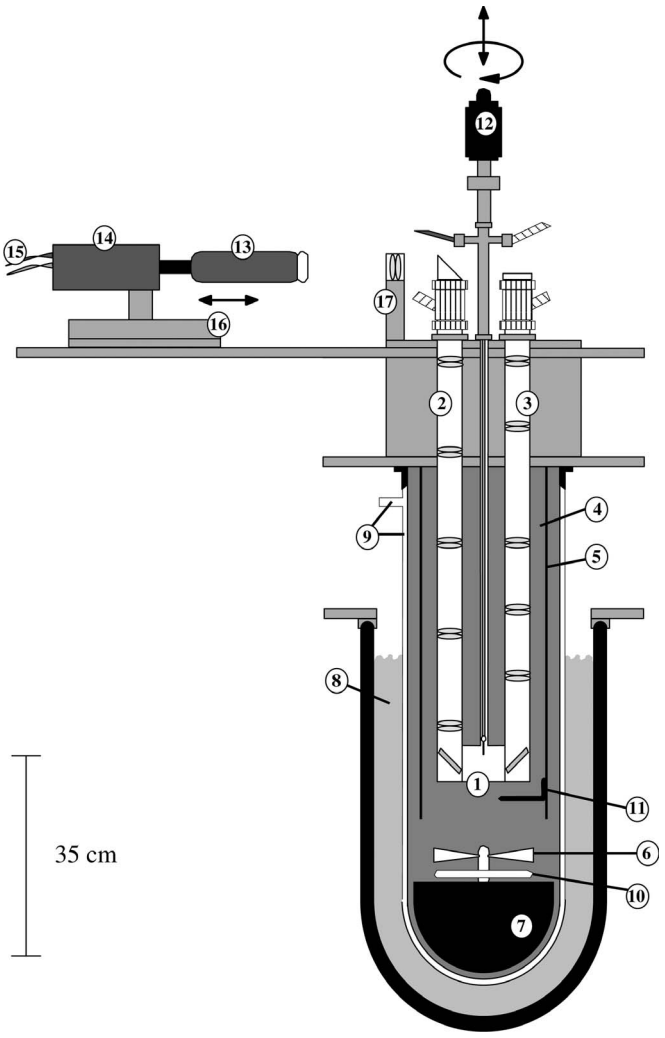

FIG. 4. Experimental setup: (1) Growth vessel with the capillary; (2) periscope; (3) illumination system; (4) heat bath (isopentane); (5) tube to provide laminar flow in the heat bath; (6) stirrer; (7) mass of stainless steel to reduce the vibrations of the stirrer; (8) liquid nitrogen; (9) adjustable helium gas atmosphere to control the cooling power; (10) heater; (11) temperature sensor; (12) combined rotary and linear motion drive to rotate and lift the capillary; (13) zoom lens (1×–7×); (14) digital CCD camera; (15) output to the computer interface and power supply for the camera; (16) high precision linear positioning system; (17) field lens.

III. EXPERIMENTAL SETUP

The cryostat (Fig. 4) consists of a double-walled glass vessel, which is filled with isopentane, and an outer vessel filled with liquid nitrogen, serving as cooling substance. Isopentane is used as thermostating medium. It is liquid over a wide temperature range and it is transparent. An adjustable helium gas atmosphere allows to control the heat flux from the isopentane to the nitrogen. A stirrer in the isopentane produces a laminar flow to achieve a homogenous temperature distribution around the growth vessel. The temperature of the isopentane is measured by means of platinum resistors (Pt 100) and controlled by electrical heaters and a proportional integral differential controller (PID).

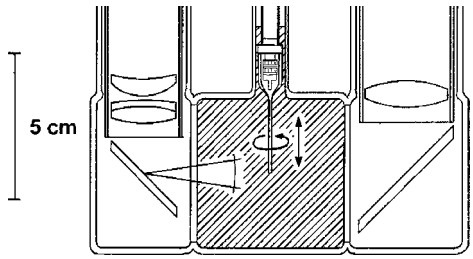

FIG. 5. Three chamber system of the growth vessel: The crystal grows in the middle chamber with a volume of about 100 cm^3. The left-hand and right-hand chambers contain optical systems for the *in situ* observation of the growth.

The growth vessel is immersed in the isopentane and filled with highly purified xenon (99.999999%). The uniform temperature T_∞ of the melt at the beginning of a growth experiment is in the range of 30 mK $\leqslant \Delta T \leqslant$ 230 mK below the triple point temperature T_t=161.3897 K, corresponding to an undercooling of about $10^{-3} \leqslant \Delta \leqslant 10^{-2}$ in dimensionless units. The temperature of the liquid xenon is measured by another Pt 100 resistor and can be controlled to $\pm 10^{-4}$ K.

We use the capillary injection technique [18] to grow three-dimensional xenon crystals from pure undercooled melt. A thin capillary is reaching into the growth vessel (Fig. 5). The volume of the growth vessel is about 100 cm^3 which provides conditions compatible with free growth. A detailed discussion of typical length scales and the proof that the assumption of "free growth" is given has been presented in Ref. [19]. By means of a Peltier element above the top of the capillary we locally achieve an undercooling sufficient to induce the nucleation of a seed. The crystal grows down through the capillary and at the end of the capillary it starts to grow freely into the surrounding melt with the uniform temperature T_∞. The long and thin geometry of the capillary ensures that only one crystal leaves the capillary. All experiments are performed with single crystals.

At the beginning of free growth a cluster of small tips starts to evolve around the tip of the capillary. After a transient state typically five dendrites develop and start to grow freely along the directions of the crystallographic axes.

We use a self-built optical system for the *in situ* observation of the growing crystal. It consists of two periscopes, one to illuminate the crystal by means of a spatially homogeneous cold light source, and a second one to capture images by a high resolution digital CCD camera (1280 $\times$ 1024 pixels at 12 Bit) at discrete time steps (1–5 s) and at the same time by an analog PAL-SVHS video recorder (25 fps at 768 $\times$ 576 pixels) for continuous recording of the growth. The optical resolution of the periscope was tested to be 1.22 μm.

The capillary is fitted to a feedthrough mechanism which provides a linear drive along the z axis and allows to turn the crystal. Using a high precision linear positioning system we can move the camera in lateral direction (x axis) to position the crystal in the field of view and along the optical axis (y axis) to focus the crystal. When a crystal grows, there is always one main dendrite with its growth direction close to the downward vertical direction. This branch can be observed for a longer time than the other branches because the capillary can be shifted in the z direction over several centimeters.

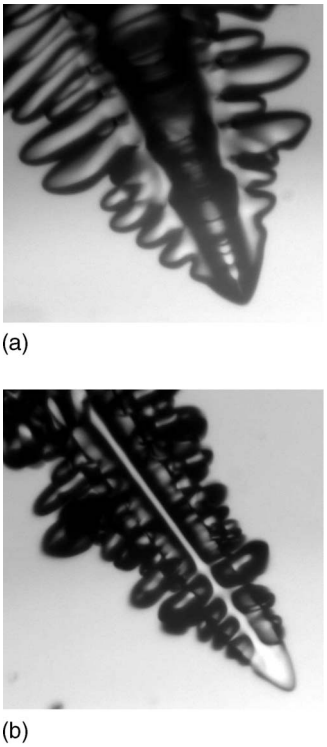

FIG. 6. Two different images of the same dendrite: (a) One symmetry plane is oriented to have maximum projection area in the image plane and (b) the dendrite turned by about 45°.

IV. METHODS

A. Image processing

The images of the crystals must be processed in order to become accessible for a numerical data analysis. A first step is the contour extraction. In a second step the contours must be transformed back to the original proportions of the crystal.

For contour extraction the contrast is enhanced. This is done by a linear interpolation of the grey levels between two boundaries called "lowcol" and "highcol." All values equal to or below lowcol or above highcol are set to black or white, respectively. Then the images are filtered by convolution with a Laplacian of a Gaussian (Marr-Hildreth operator) [20]. Using a threshold strategy the filtered images are searched for zero crossings resulting in edges that are 1 pixel thick.

Since the transparent crystal is illuminated by a diffuse light source from the rear, the image obtained from the crystal is actually an image of the light source seen through the crystal. Refraction of light at the crystal surface provides the images in our experiments (Fig. 6). The intensity of the light that leaves the crystal and reaches the image sensor depends strongly on the orientation of the crystal surface where light is refracted. Regions of the crystal where light passes

through the crystal without or with only small refraction appear white. Regions where the surface is parallel to the observation direction appear dark. Since the observed crystals have complex shapes the images show many bright and dark regions. Therefore not only the outside contour, but also edges inside the crystal area found by the edge detection technique described above. From all these edge lines the longest one is considered to be the contour of the crystal. A detailed description of the contour extraction procedure can be found in Ref. [21].

Sidebranches grow in the two symmetry planes which are normal to each other and perpendicular to the growth direction of the main tip. They can be seen without geometrical deformation if one symmetry plane is parallel to the object plane of our periscope. The dendrites usually do not grow along the direction of the capillary. Therefore these conditions are not given in most cases. By turning the capillary around the vertical axis we can orient two fins into the plane perpendicular to the object plane of the periscope. After orienting the crystal in this way, the sidebranches growing in the plane perpendicular to the image plane appear as bright spots. The structure of the sidebranches growing in the other symmetry plane can still be seen although the projection is not normal. Figure 6 shows two images of the same dendrite, one in the maximum projection area orientation (a) and after turning it about 45° (b).

Since there is a nonvanishing angle between the growth direction and the object plane, the images taken from these projections do not show the dendrites in its original proportions. In order to obtain contours with the original proportions of the crystals they must be transformed back with a transformation matrix. The values needed to calculate this matrix are the angle α_1 between the vertical axis and the growth direction of the dendrite in the image that must be transformed, and a second angle α_2 between the vertical axis and the growth direction of the dendrite in a second projection after turning the crystal 90° around the vertical axis. Schematically the two projections of a dendrite with the two angles are given in Fig. 7, left-hand side. After the transformation $T(\alpha_1,\alpha_2)$ the dendrite can be seen in its original proportions (Fig. 7, right-hand side). An example of a dendrite with its contour and the contour rescaled and centered is given in Fig. 8. A detailed description of this procedure can be found in the Appendix.

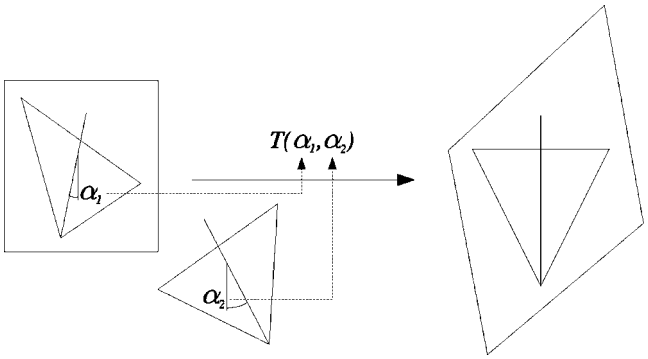

FIG. 7. Schematic of the back transformation. Left-hand side, the projections of a dendrite that must be transformed, and a second projection needed to calculate the transformation matrix $T(\alpha_1,\alpha_2)$. The angles α_1 and α_2 are taken between the vertical direction and the growth direction of the two projections of the dendrite. Right-hand side, the dendrite after transformation in its original proportions. Details of the procedure are given in the Appendix.

B. Positions of tips

The main tip and the tips of active sidebranches are the fastest moving points of a dendrite. They can be interpreted as local maxima of the velocity of the moving crystal interface. We use this property to automatically determine the evolution of the tip positions.

We start from the contour S_N of the last image and manually select the sidebranch tip points $\mathbf{P}_{N,j}$. This can also be done automatically by selecting the points where the contour has a local maximum in the curvature and where the curvature is above a certain threshold.

Starting with the last contour ($i=N$) we find the preceding points $\mathbf{P}_{i-1,j}$ by iteration and the condition

$$|\mathbf{P}_{i,j}-\mathbf{P}_{i-1,j}| = \min_{\mathbf{v}\in S}|\mathbf{P}_{i,j}-\mathbf{v}|. \tag{8}$$

Figure 9 shows three contours and the arrows connecting the positions of the tips.

C. Half-widths and sidebranch activity of the dendrite tip

For a transformed and centered dendrite contour the half-width $x(z,t)$ is defined as the absolute value of the horizontal distance from the z axis to the contour at a given distance from tip z and for a given t (Fig. 10).

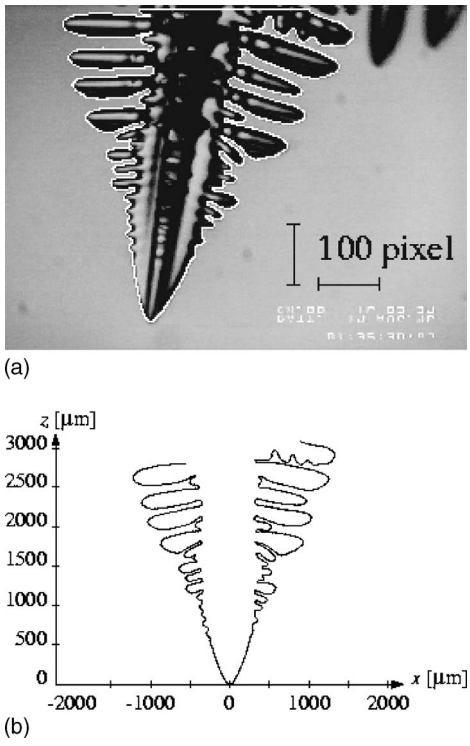

FIG. 8. Image processing. (a) Dendrite with overlaid contour. (b) Contour after transformation to the original proportions and shifting the oriented contour to the origin of the coordinate system.

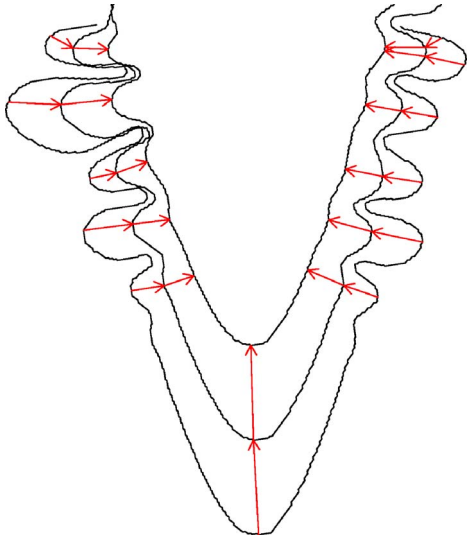

FIG. 9. (Color online) Tracing the positions of the sidebranch tips: Beginning from a contour S_i with known tip positions $\mathbf{P}_{i,j}$, the corresponding tip positions $\mathbf{P}_{i-1,j}$ of the preceding contour S_{i-1} can be found by determining the point of S_{i-1} with the minimal distance from point $\mathbf{P}_{i,j}$.

Figure 11(a) shows a 2D plot of the two half-widths of a contour sequence. Red (dark gray) and yellow correspond to the minimum and to the maximum absolute values of x, respectively. The half-width at a given distance from the tip oscillates around its mean value. The increase of the amplitude of these oscillations with z corresponds to the increasing size of the sidebranches. In the plot sidebranches can be identified with the bright sloped lines. These lines vanish with decreasing distance from tip (small z).

In order to make fluctuations at small z also visible, we define the sidebranch activity $\tilde{x}_z(t)$ as the normalized amplitude of $x(z,t)$ around its mean value $\langle x(z,t)\rangle_t$. Normalized means that the values within a given z are divided by the maximum absolute value for this z, limiting these values to $\max|\tilde{x}_z(t)|=1$. Plotting the sidebranch activity in a 2D plot [Fig. 11(b)] reveals the fluctuations of the sidebranches at all distances from the tip at full color range. Even small fluctuations corresponding to the beginning of sidebranch growth can be traced down to their first appearance. This allows us to measure the distance behind the tip at which a sidebranch starts to grow.

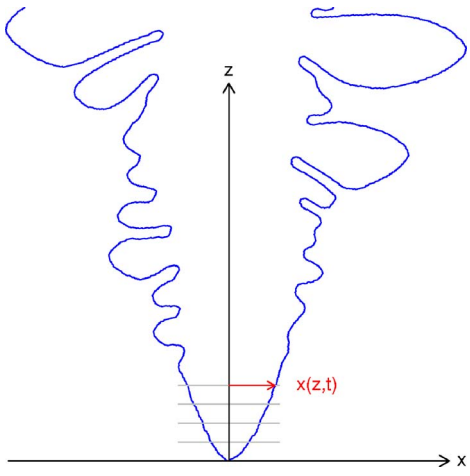

FIG. 10. (Color online) Half-width $x(z,t)$ of the right-hand side of a dendrite contour.

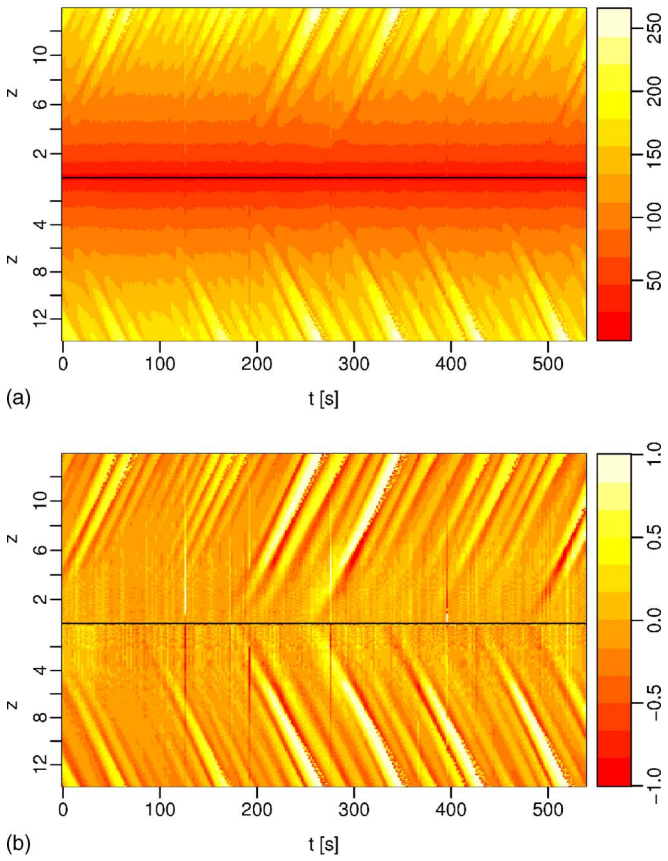

FIG. 11. (Color online) Half-width and sidebranch activity. (a) Two-dimensional plot of the half-widths $x(z,t)$ of a contour image sequence. (b) Sidebranch activity $\tilde{x}_z(t)$ of the same sequence. It is defined as the normalized amplitude of $x(z,t)$ around its mean value $\langle x(z,t)\rangle_t$ calculated separately for each z. Red/dark corresponds to −1, yellow to 1.

V. RESULTS

A. Onset and amplitude of sidebranches

In this paragraph we compare experimental results with the predictions of the rigorous calculations of Brener *et al.* [13,22]. Based on the mechanisms which initiate sidebranches we distinguish two types: type N sidebranches which are initiated by the selective amplification of thermal noise, and type P sidebranches which are initiated by macroscopic perturbations of the dendrite tip.

1. Sidebranches induced by selective amplification of thermal noise (type N)

The initiation of type N sidebranches has been studied in some detail for axisymmetric dendrites, for a review see Ref. [23]. An important step forward was made by Brener and

Temkin [13,22] who determined the shape of the tip and the sidebranch amplitude of 3D non-axisymmetric crystals analytically. The sidebranch amplitude was found to be

$$A_{\mathrm{BT}}(z) = \langle \xi_1^2(z) \rangle^{1/2} \approx \bar{S} \exp\left(\frac{2(5/3)^{9/10}}{3\sqrt{3\sigma^*}} z^{2/5} \right), \tag{9}$$

where $\bar{S}^2 = 2k_B T^2 c_{p,l} D/(L^2 v_{\mathrm{tip}} R^4)$ is the dimensionless noise or fluctuation strength and $\sigma^* = 2Dd_0/(v_{\mathrm{tip}} R^2)$ the so-called stability constant with the capillary length $d_0 = \gamma_{\mathrm{sl}} c_{p,l} T_m / L^2$. Where D, v_{tip}, R, γ_{sl}, $c_{p,l}$, T_m, L are the thermal diffusivity, the tip velocity, the tip radius, the free energy of the solid-liquid interface, the specific heat, the equilibrium melting temperature and the latent heat of melting, respectively. The material properties used to calculate the fluctuation strength $\bar{S}$ and the stability constant σ^* can be found in Ref. [5]. The ΔT dependence of the tip radius and the tip velocity was determined by Hürlimann [5],

$$R = (5.2 \pm 0.4) \times 10^{-3} \Delta T^{-0.83 \pm 0.03},$$

$$v_{\mathrm{tip}} = (1.888 \pm 0.086) \times 10^{-1} \Delta T^{1.745 \pm 0.017}, \tag{10}$$

where R is given in μm, v_{tip} in μm/s, and ΔT in K.

Bisang and Bilgram [11] compared the shape of the tip and the amplitudes of sidebranches of experimentally grown three-dimensional xenon dendrites with the predictions made in Ref. [13]. They used the mean distance $\bar{z}_{\mathrm{sb}}$ between the tip and the position where the sidebranches have a root-mean-square amplitude

$$A_{\mathrm{exp}}(z) = \sqrt{\langle [x(z,t) - \langle x(z,t) \rangle]^2 \rangle} \tag{11}$$

of about $1R$. According to Brener and Temkin [13] this position behind the tip is

$$\bar{z}_{\mathrm{sb}}(1R) \approx \frac{(27\sigma^*)^{5/4}}{2^{5/2}\left(\frac{5}{3}\right)^{9/4}} |\ln \bar{S}|^{5/2}. \tag{12}$$

$\bar{z}_{\mathrm{sb}}$ was found not to depend on undercooling and the mean value was $\bar{z}_{\mathrm{sb}} = 17.5 \pm 3$ in units of R, which is in quantitative agreement with the theory.

The plot of the sidebranch activity of a sequence reveals whether the dendrite grows in a steady state or sidebranches have been induced by macroscopic perturbations. The tip shape of a dendrite growing in a steady state can be described by a 5/3 power law deduced in Ref. [22]. Type N sidebranches are silhouetted against the noise at about 3–7 tip radii R behind the tip. Figure 12 shows the sidebranch activity $\tilde{x}_z(t)$ of a typical type N dendrite sequence (Sec. IV C), plotted in colors (from red=−1 to yellow=+1) vs time t (horizontal axis) and distance from tip z (vertical axis). The upper part of the plot corresponds to the left-hand side and the lower part to the right-hand side of the dendrite. We analyzed about 30 sequences of dendrites grown in a steady state. Sequences with sidebranches appearing at the tip ($z < 3$) have been excluded in this analysis. They will be analyzed in Sec. V A 2.

Figure 13(a) shows a linear plot of the sidebranch amplitude $A_{\mathrm{exp}}(z)$ vs distance from tip z of a steady state dendrite

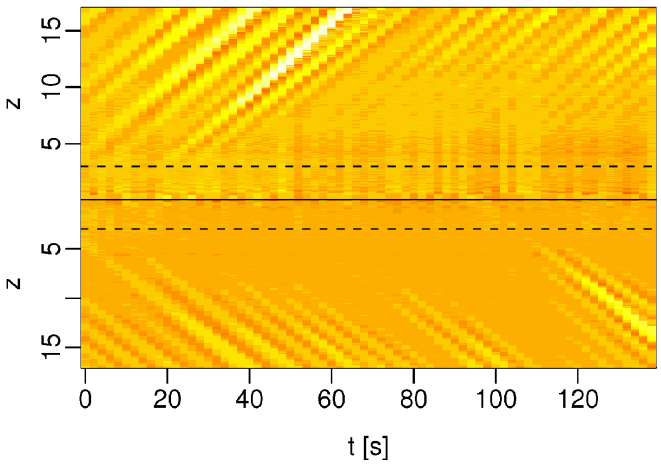

FIG. 12. (Color online) Type N sidebranch initiation by noise: Two-dimensional plot of the sidebranch activity $\tilde{x}_z(t)$ of a typical dendrite. Values range from −1 (red/dark) to 1 (yellow). The dashed lines drawn at $z=3$ show the border where the first indications for sidebranches can be observed.

sequence. In order to compare this curve with the prediction given in Eq. (9), we rewrite this equation to

$$\ln A(z)_{\mathrm{BT}} \approx \ln \bar{S} + \frac{2(5/3)^{9/10}}{3\sqrt{3\sigma^*}} z^{2/5}. \tag{13}$$

Plotting $A_{\mathrm{exp}}(z)$ on a logarithmic scale vs $z^{2/5}$ [Fig. 13(b)], a straight line denotes a linear dependence of $\ln A(z)$ on $z^{2/5}$

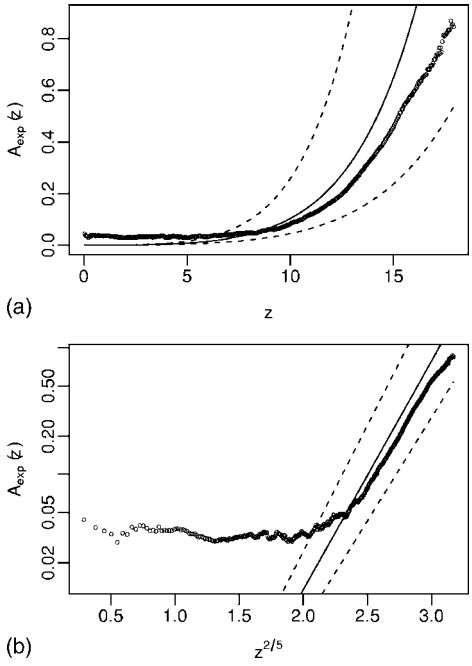

FIG. 13. Root-mean-square amplitude $A_{\mathrm{exp}}(z)$ of type N sidebranches of a dendrite grown at $\Delta T = 144$ mK. The solid drawn lines are $A_{\mathrm{BT}}(z)$ calculated with the values of R and v_{tip} from Eqs. (10) and the dashed lines correspond to the uncertainties given in (10). (a) Dimensionless coordinates on a linear scale. (b) $A(z)$ plotted on a logarithmic scale vs $z^{2/5}$ according to Refs. [13,22].

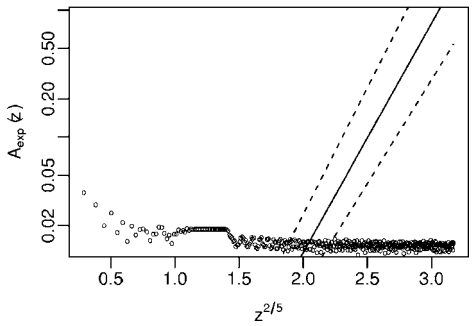

FIG. 14. Noise originating from pixel grid. $A_{exp}(z)$ of synthetic contours with no sidebranches. The synthetic contours were produced by projecting a curve of the form $z=a|x|^{5/3}$ onto a pixel grid (rounding the coordinates to integers). The orientation and the positions of the curves, the pixel size and the tip radius correspond to the values of the experimental contour sequence of Fig. 13(b). The finite values measured here result from irregular fluctuations originating in the principally limited representation of smooth curves in a discrete pixel grid.

according to Eq. (13). The proportionality is given by $2(5/3)^{9/10}/(3\sqrt{3\sigma^*})$. The solid line in these plots corresponds to the theoretical value $A(z)_{BT}$ derived from the values R and v_{tip} from Eqs. (10) and the dashed lines enclose the regions of uncertainties. We point out that we compare experimental data directly with the rigorous calculations of Brener *et al.* [13,22]. We do not analyze by means of a log-log plot, but we plot the data in a $z^{2/5}$ scale given by the theory. The straight line in Fig. 13(b) is derived from theory. There are no free parameters. Each of the points plotted in Fig. 13 is a result of the analysis of 50 to 300 contours.

The tested sequences are within the limits of uncertainties. The measured amplitudes are below $0.1R$ (<2 μm) for $z<7R$. The noise level in this region is likely an artefact due to the pixel-based contour extraction of the digital images and does not depend on z. For a comparison, the root-mean-square amplitude originated only by the discrete pixel grid is given in Fig. 14. To generate this plot, a sequence of synthetic contours with no sidebranches was produced. The same tip radius was used as the radius of the sequence of Figs. 13(a) and 13(b). The contours were rendered at the same pixel-resolution and the same calculations were applied to the contours in order to get $A_{exp}(z)$.

2. Sidebranches induced by macroscopic perturbations (type P)

According to Ref. [15] we interpret the growth of sidebranches starting to grow immediately after the dendrite tip as the result of perturbations. Such type P sidebranches can also be induced by a mechanical shock to the system or vibrations applied to the cryostat vessel. The sidebranch activity of a dendrite sequence with type P sidebranches is given in Fig. 15(a). The half-widths $x_{left}(z,t)$ and $x_{right}(z,t)$ at $7R$ (corresponding to about $z=200$ μm) are plotted vs time in Fig. 15(b). The vertical displacement of the tip around its average steady state position as a function of time $\Delta z_{tip}(t)=z(t)-v_{tip}\,t$ (perturbation shift) is plotted below. The t axis of the x vs t plot has been shifted to the left-hand side by Δt

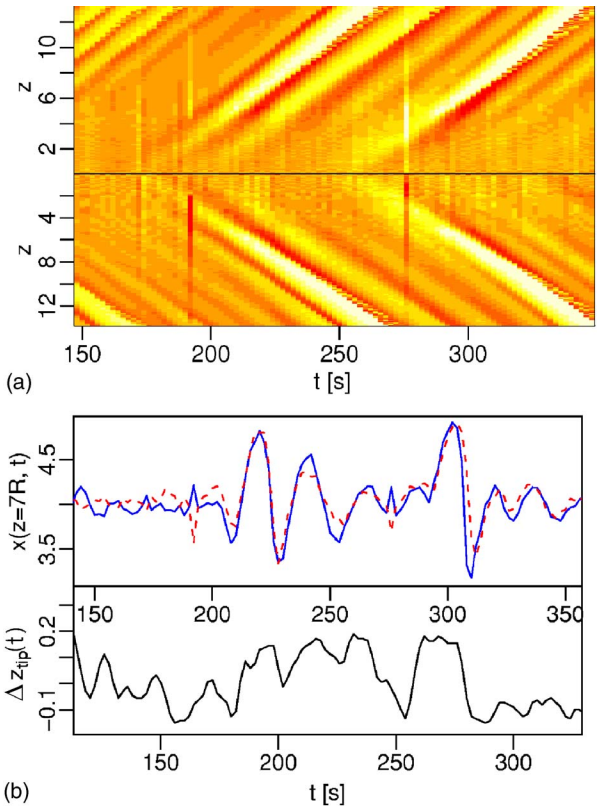

FIG. 15. (Color online) Type P sidebranches initiated by macroscopic perturbations. (a) 2D plot of the sidebranch activity $\tilde{x}_z(t)$ of a dendrite sequence with type P sidebranches. (b) The half-widths $x_{left}(z,t)$ and $x_{right}(z,t)$ at $z=7R$ (corresponding to about 200 μm) are plotted vs time (left-hand side, solid blue; right-hand side, dashed red). The vertical displacement of the tip $\Delta z_{tip}(t)$ (perturbation shift) is plotted below (the upper time scale is shifted against the lower one by 25 s). This corresponds to the time the crystal takes to grow a distance of about $4.4R$ (125 μm). The perturbations can be compared to a local perturbation at $z\simeq 7R-4.4R=2.6R$ (75 μm) behind the tip.

$=25$ s, which corresponds to about $\Delta z=v_{tip}\Delta t\simeq 4.4R$ (125 μm). Both curves $x_{left}(z,t)$ and $x_{right}(z,t)$ show large fluctuations corresponding to the symmetric sidebranches observed in the plot of the sidebranch activity given in Fig. 15(a). They are similar to the perturbation shift observed 25 s earlier. The effect of the perturbation can be compared to a local perturbation at $z\simeq 7R-4.4R=2.6R$ (75 μm) behind the tip.

Also convectional flow or uncontrolled perturbations can lead to the growth of type P sidebranches. Figure 16(a) shows three images of a dendrite where sidebranches began to grow close to the tip. Figure 16(b) shows the sidebranch activity of a similar sequence where sidebranches started to grow at the tip at $t=100$ s. At about $t=250$ s the dendrites returned to a steady-state mode where sidebranches became again visible at about $5R$.

B. Tip positions of sidebranches

In Fig. 17, selected shape and growth parameters characterizing a dendrite are shown. The gray solid line is the con-

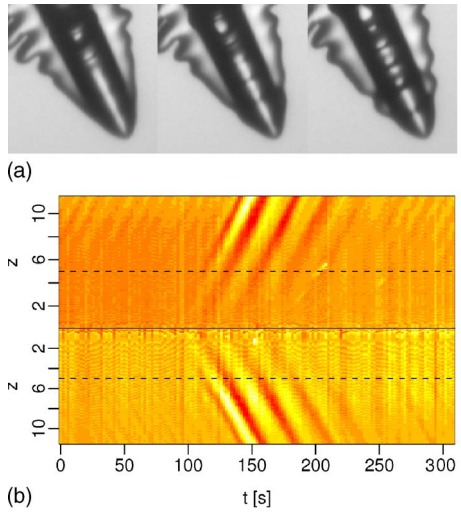

FIG. 16. (Color online) Transient from type N to type P. (a) After a perturbation of a dendrite with a smooth tip, the dendrite begins to produce sidebranches at the tip on all four fins. (b) Sidebranch activity of a dendrite with a smooth tip (type N) that begins to produce sidebranches at the tip at $t=100$ s (type P) and again becomes a dendrite with a smooth tip (type N) at about $t=250$ s.

tour of a dendrite. The dendrite grows along the negative z axis $\langle 100\rangle$ with tip velocity v_{tip}. A circle at the tip with a radius according to the radius of curvature at the tip (tip radius R) illustrates the length scale of the dendrite. The sidebranches grow approximately along the direction of the maximum thermal gradient at a velocity v_{sb}. This growth direction is characterized by α_{sb}, it is not exactly parallel to $\langle 010\rangle$ or $\langle 001\rangle$. The positions of the sidebranch tips in a coordinate system with its origin at the dendrite tip can be characterized by the local slope $m_{\mathrm{sb}}(z)=\Delta x(z)/\Delta z(z)$ at a given distance z behind the dendrite tip. We do not find any evidence that the slope $m_{\mathrm{sb}}(z)$ depends on undercooling. This is in agreement with the assumption that dendrites grown at different undercoolings are similar. The mean opening angle Φ describing the envelope of the dendrite is calculated from the mean of the opening angles Φ_{sb} of active sidebranches. The mean opening angle Φ_{sb} of a sidebranch is calculated from the mean slope $\bar{m}_{\mathrm{sb}}$ of a sidebranch:

$$\Phi_{\mathrm{sb}}=\tan^{-1}|\bar{m}_{\mathrm{sb}}|. \tag{14}$$

The analysis in Sec. V A is limited to a distance of some tip radii behind the dendrite tip [13]. Using the tip positions it is possible to characterize the growth of sidebranches at much larger distances and to look at individual sidebranches. In order to track tip positions it is necessary to have long sequences where several sidebranches can be observed from their first appearance until they have grown to the length of many tip radii. Only active sidebranches will be taken into account in the following.

To obtain first information we have selected three contour sequences at undercoolings $129\ \mathrm{mK}\leqslant T_{\infty}\leqslant 218\ \mathrm{mK}$ $(0.0025\leqslant\Delta\leqslant 0.0042)$ and orientation angles below 19° that show no significant asymmetry between the two sides in sidebranch growth. In Fig. 18(a) traces of the tip positions of

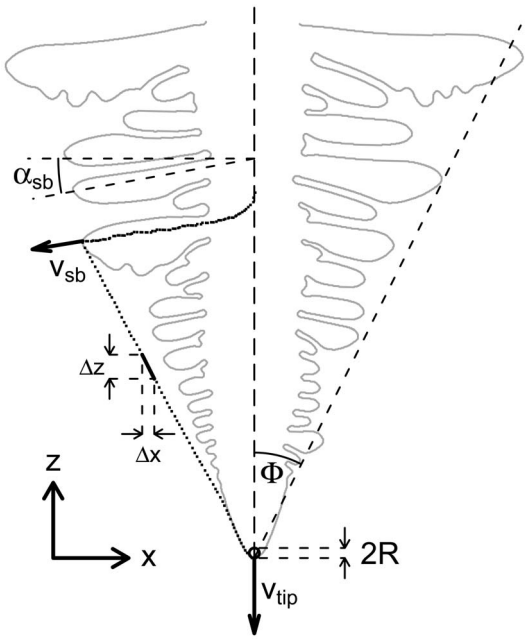

FIG. 17. Selected shape and growth parameters characterizing the growth of sidebranches far behind the dendrite tip. The growth velocity v_{sb} of the sidebranches and their orientation angle α_{sb} are determined from the sidebranch tip positions in the laboratory coordinate system. The positions of the sidebranch tips in a coordinate system with its origin at the dendrite tip can be characterized by the slope $m_{\mathrm{sb}}(z)=\Delta x(z)/\Delta z(z)$ at the distance z behind the dendrite tip. The dotted line traces the tip positions of this sidebranch relative to the dendrite tip as it develops with time. The mean opening angle Φ is the average of the opening angles Φ_{sb} of the individual sidebranches, averaged over an interval $[z_1,z_2]$.

the active sidebranches of these sequences are plotted. They lie in two distinct bunches. The dashed line in Fig. 18(a) corresponds to

$$x=0.5z, \tag{15}$$

which separates these two bunches. From 30 sidebranches six grow significantly above this line while 24 grow below. We have found in comparisons of sidebranch activities with the sidebranch tip positions that sidebranches corresponding to the upper bunch are all type P sidebranches, while sidebranches corresponding to the lower bunch are type N sidebranches.

In Fig. 18(b) the traces of the slopes of the tip positions are plotted. The dashed line in Fig. 18(b) corresponds to the constant slope $m=0.5$ of the dashed line plotted in Fig. 18(a). The theoretical dendrite tip shape without sidebranches is given by Eq. (1). Using the definition of the tip radius given in Ref. [7], the shape can be written in dimensionless coordinates as

$$x=2^{2/5}z^{3/5}. \tag{16}$$

The dotted line in Fig. 18(b) corresponds to the slope of this curve. Again sidebranches of type N and type P lie in two separate bunches that can be well distinguished. Type P sidebranches deviate from this line at about $5R$ behind the den-

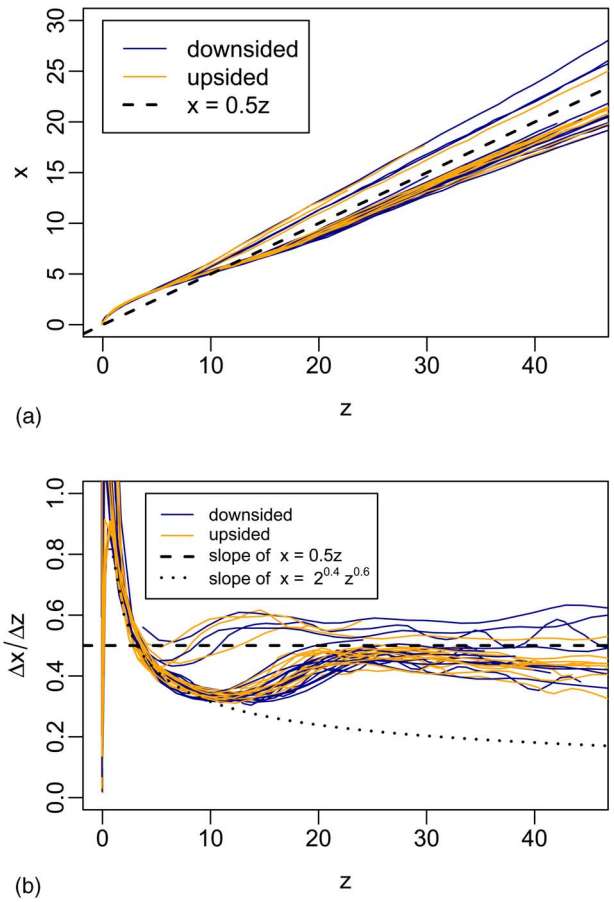

FIG. 18. (Color online) Symmetric sidebranches at small orientation angles. (a) The positions $x(z)$ of the sidebranches of three different dendrites at undercoolings 129 mK$\leqslant T_\infty \leqslant$218 mK ($0.0025 \leqslant \Delta \leqslant 0.0042$) have been superimposed. The angles α_1 and α_2 of these selected sequences are below 19°. The positions of the downsided (blue/dark) and the upsided (orange/bright) sidebranches all lie in two bunches separated by the dashed line $x=0.5z$. In (b) the slopes $m_{sb}(z)$ of the positions $x(z)$ are plotted against z. Low values of the slopes correspond to low growth rates, high slopes to high growth rates. The lines separate into two distinct sidebranch types. The upper bunch corresponds to type P and the lower bunch to type N sidebranches, separated by the dashed lines (constant slope $m=0.5$). The dotted line is the slope of a theoretical 5/3 dendrite tip without sidebranches.

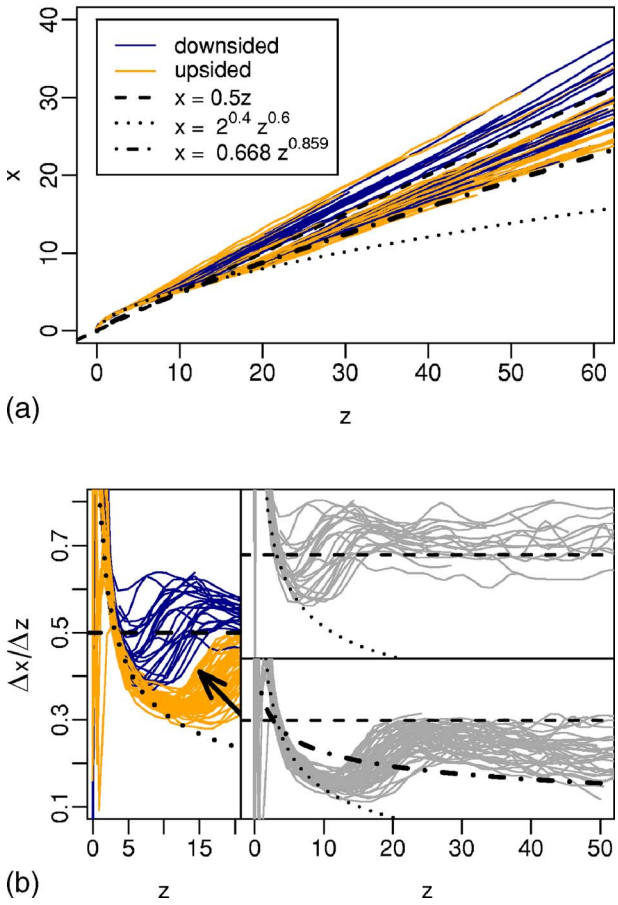

FIG. 19. (Color online) Two sidebranch modes for dendrites at small orientation angles. (a) Superimposed sidebranch tip positions of seven sequences at different undercoolings (129 mK$\leqslant T_\infty \leqslant$218 mK) and angles α_1 and α_2 below 19°. The downsided sidebranches are plotted in blue (dark), the upsided branches in orange (bright). Below the dashed line $x=0.5z$ a gap separates type P sidebranches from type N sidebranches, which is marked in (b) by the arrow. This is an experimental observation. We will be happy about a theoretical discussion about this gap. The dotted curve is the shape of an undisturbed dendrite tip. The dashed-dotted curve corresponds to the envelope obtained by Li and Beckermann. (b) Plots of the slopes of sidebranch positions. Here the different types are plotted in different colors: N in blue (dark) and P in orange (bright). The gap separating the two types is indicated by the arrow. On the right-hand side the two distinct branches of type P and type N sidebranches are plotted separately. At a larger z scale almost all values of type P sidebranches are larger than 0.5 and all values of type N sidebranches below 0.5.

drite tip and the slopes quickly saturate at about $15R$. Sidebranches lying in the lower bunch (type N) separate at about $10R$ and saturate approximately at $25R$ at the latest (see Fig. 18). In the range $25-35R$ behind the tip the slopes of all sidebranches remain approximately constant and we calculated the mean values from values within this interval.

In the following we take four additional sequences into account which show a slight asymmetry between the downsided and the upsided sidebranches due to convection. The undercooling and the orientation angles of the additional sequences are within the same limits as before. Although there is an asymmetry we find the same separation of the type N and type P sidebranch modes [Figs. 19(a) and 19(b)]. This gap is marked by an arrow. The gap indicates that there is not a continuous transition from type N to type P but an instability. Again the $m=0.5$ line is a lower limit for type P sidebranches. Li and Beckermann [24] fitted the envelope of active sidebranches of pure succinonitrile dendrites grown under microgravity conditions by

$$x = 0.668 z^{0.859}. \tag{17}$$

This curve corresponds to the dashed-dotted line plotted in Fig. 19(a), and its slope to the dashed-dotted line in Fig. 19(b). It fits to the positions and the slopes of the slowest type N sidebranches. Therefore it can be considered to be a

TABLE I. Comparison of the fitting parameters $x=\alpha z^{\beta}$ of the envelope of succinonitrile (SCN) dendrites grown under convection-free (cf) microgravity conditions [24], of pivalic acid (PVA) [2] and SCN dendrites [3] grown under convection-free (cf) and diffuso-convective (dc) conditions. We compare our data to the values fitted by Li and Beckermann.

		Giummarra *et al.* [2]		Corrigan *et al.* [3]	
Reference	Li *et al.* [24] SCN, cf	PVA, cf	PVA, dc	SCN, cf	SCN, dc
α	0.668	0.87±0.26	0.65±0.19	0.603	0.519
β	0.859	0.73±0.09	0.82±0.09	0.852	0.920

lower limit for the growth of type *N* sidebranches growing downward. The data used by Li and Beckermann [24] have also been analyzed by Giummarra *et al.* [2]. The data for the $x=\alpha z^{\beta}$ are collected in Table I. The slopes of almost all type *N* sidebranches are slowly decreasing with distance from the tip [Fig. 19(b)] whereas the slope of the type *P* sidebranches remain constant or even increase.

Figures 19(a) and 19(b) show that the earlier a sidebranch starts the faster it grows. The order of appearance corresponds mostly to the order of tip speeds and the size of the sidebranches. Sidebranches initiated close to the tip by perturbations (type *P*) grow faster than sidebranches initiated some distance from the tip by thermal fluctuations (type *N*). This is because the thermal gradient in the melt is highest at the dendrite tip and decreases with increasing distance from the tip. Figure 3 illustrates the isotherms around a dendrite tip.

The dashed line at 0.5 separates type *P* from type *N* sidebranches: Almost all type *P* sidebranches have a slope larger than 0.5, while the slopes of all type *N* sidebranches are below 0.5. Also the more the slope of a sidebranch after saturation lies above or below 0.5 the more it will increase or decrease with distance from the dendrite tip. Slopes being close to 0.5 will stay almost constant at this level.

In Table II the mean values of the slopes $\langle \bar{m}_{\mathrm{sb}} \rangle$, the opening angle Φ and the sidebranch orientation $\langle \alpha_{\mathrm{sb}} \rangle$ are given. In Ref. [25], Kaufmann analyzed the sidebranch development of xenon dendrites. In this work it was not distinguished between type *P* and type *N* sidebranches. For a comparison the mean values calculated from all active sidebranches are listed in the following. The mean slope is found to be

$$\langle \bar{m}_{\mathrm{sb}} \rangle_{\mathrm{all}} = 0.47 \pm 0.06, \tag{18}$$

corresponding to the mean opening angle

$$\Phi = 25^{\circ} \pm 3^{\circ}. \tag{19}$$

The mean orientation angle of the sidebranches is

$$\langle \alpha_{\mathrm{sb}} \rangle = 10^{\circ} \pm 5^{\circ}. \tag{20}$$

These values are in agreement with the values found by Kaufmann. This demonstrates the high degree of reproducibility of sidebranch behavior.

C. Envelope of a dendrite

The envelope of a dendrite can be defined as the line connecting the outermost points described by all centered contours of a dendrite. It is the smallest shape including all centered contours of a dendrite. The envelope of a dendrite can be described by three regions (Fig. 20):

A first region (I) is the tip region where no sidebranches appear. The shape of the tip can be described by the power law given in Eqs. (1) and (16). The results from Sec. V B show that the distance z_1 where sidebranches begin to influence the envelope of a dendrite, ranges from $5R$ for type *P* sidebranches to about $10R$ for type *N* sidebranches.

After sidebranches become visible at some distance behind the tip, the slopes of their tip positions are relatively constant over a large interval of distances behind the dendrite tip as shown in Figs. 18(b) and 19(b). This region of the envelope (II) can be described by a straight line. The detailed shape of the crossing between these two regions has not been determined. For sidebranches at small orientation angles and taking all sidebranches into account, region II of the envelope is described by

$$x = m_{\mathrm{all,max}} z \approx 0.6z. \tag{21}$$

If we consider only type *N* sidebranches to contribute to the envelope, it is described well by

$$x = m_{N,\mathrm{max}} z = 0.5z. \tag{22}$$

TABLE II. The mean values corresponding to Fig. 19. $\langle \bar{m}_{\mathrm{sb}} \rangle$ is the mean slope, Φ the mean opening angle and $\langle \alpha_{\mathrm{sb}} \rangle$ the mean sidebranch orientation angle of the active sidebranches. The means have been calculated from the values in the interval $25-35R$ behind the tip. *n* is the number of contours.

Selection	$\langle \bar{m}_{\mathrm{sb}} \rangle$	Φ	$\langle \alpha_{\mathrm{sb}} \rangle$	*n*
All	0.47±0.06	25°±3°	10°±5°	74
Type *P*	0.54±0.05	28°±3°	9°±5°	21
Type *N*	0.44±0.04	24°±2°	11°±5°	53

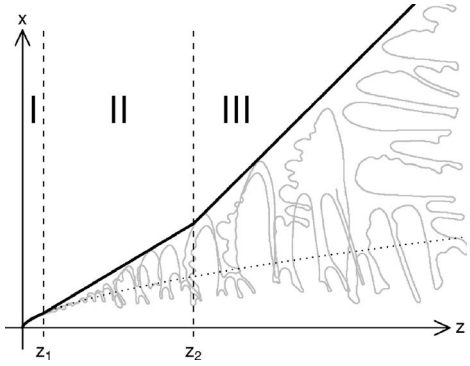

FIG. 20. Schematic of the envelope of dendritic growth. One can distinguish three different regions: (I) The dendrite tip region is described by a power law $\hat{x}=a\hat{z}^{3/5}$. (II) The region where the sidebranch tip velocities are approximately constant, and (III) the region where the largest sidebranches become freely growing dendrites. The position z_1 at the border between (I) and (II) ranges from about $3R$ for type P sidebranches to about $20R$ for type N sidebranches. The border between (II) and (III) is not sharp and varies from dendrite to dendrite. For the analyzed dendrites we estimate z_2 to be in the range $30R-50R$.

At larger distances growth velocity of the most dominant sidebranches slowly increases and they transform into individual dendrites, accompanied by the onset of tertiary sidebranches. The velocities of the sidebranches do not exceed the velocity of a steady state dendrite tip ($v_{sb} \leqslant v_{tip}$), and therefore the maximum slope is limited by 1. For the analyzed dendrites we estimate z_2 to be in the range $30R \leqslant z_2 \leqslant 50R$.

VI. DISCUSSION

A. Onset and amplitude of sidebranches

Our experimental results allow the characterization of dendrites by three parameters: (i) The distance from the dendrite tip where sidebranches start to grow, (ii) the amplitude of sidebranches as a function of the distance from the tip, (iii) the symmetry of sidebranches.

Using these parameters we can clearly identify two types of sidebranches: Sidebranches that are initiated by selective amplification of thermal noise (type N) and a new type of sidebranches, initiated by macroscopic perturbations (type P).

Type N sidebranches start to grow 3–7 tip radii behind the tip (Fig. 12) and the sidebranches growing at the four fins are not correlated. The amplitude for type N sidebranches as a function of the distance from the dendrite tip [Eq. (9)] has been predicted by Brener and Temkin [13]. Our results agree without any fitting parameters. We have verified that the sidebranch amplitude grows exponentially to $z^{2/5}$ (Fig. 13). This result confirms the selection of $\bar{S}^2$ and σ^*.

Type P sidebranches are initiated by macroscopic perturbations (e.g., by vibrations applied to the vessel of the cryostat). They start to grow at the tip and their amplitude is significantly higher than type N sidebranches. The growth of type P sidebranches is symmetric at the four fins (Fig. 15).

These results show that the initial conditions determine the growth of sidebranches (see also Ref. [26]).

B. Tip positions of sidebranches and the envelope of a dendrite

It was found that type P sidebranches can be well distinguished from type N sidebranches: A gap in the plot of the slopes clearly separates the two types [Fig. 19(b)]. Type P sidebranches separate from the surface of a dendrite [Eq. (1)] at about $5R$ and a saturation of the slopes is observed at about $15R$. Type N sidebranches separate at about $10R$ and the slopes saturate at $25R$ at the latest.

For the mean values of the slopes of type P sidebranches we find $m_{sb,P}(z) \geqslant 0.5$ and for type N sidebranches $m_{sb,N}(z) \leqslant 0.5$. The line $x=0.5z$ is found to be an upper limit for the growth of type N sidebranches and a lower limit for type P sidebranches [Fig. 19(a)]. This allows to distinguish quantitatively between undisturbed and disturbed dendrites.

The curve describing the envelope of pure succinonitrile dendrites grown under microgravity conditions [Eq. (17)] obtained by Li and Beckermann [24] is found to be a lower limit for type N sidebranches [Fig. 19(a)]. This means that all active sidebranches observed in our experiments grow at least as fast as sidebranches of dendrites grown under microgravity conditions. Natural convection acts as an accelerator for downward growing sidebranches. The upper limit for downward growing type N sidebranches is given by $x \leqslant 0.5z$.

The envelope of a dendrite (Fig. 20) can be described by three regions according to the three sidebranch growth regimes: (I) a tip region with no apparent sidebranches, where the envelope is described by the 5/3 power law, (II) a region where sidebranches grow at a constant velocity $v_{sb} \approx 0.5 v_{tip}$, corresponding to a slope of the envelope of about 0.5 and an opening angle $\Phi \approx \tan^{-1}(0.5) \approx 26.57°$, and (III) a third region where sidebranches become individual sidebranches. The maximum slope of the third region is limited by the maximum velocity of sidebranches $v_{sb} \leqslant v_{tip}$. This leads to a maximum slope of $m_{sb,max}=1$, corresponding to $\Phi=45°$.

For an explanation of the ratio between the sidebranch tip velocities and the dendrite tip velocity of $v_{sb}/v_{tip} \approx 0.5$, we consider the following arguments: Sidebranches in 3D grow at the ridges of the dendrite fins side by side. Dissipation of latent heat released by the sidebranches is limited in the regions where other sidebranches grow. A 3D dendrite can be compared with a stack of 2D dendrites growing perpendicular to the direction of the main tip. Therefore the growth conditions under which sidebranches grow can be compared to the growth of a dendrite in two dimensions. Growth of an interface is limited mainly by the diffusion of latent heat characterized by Laplace's equation, whose radial solutions are of the form r^N, with N the dimension. The latent heat condition [Eq. (4)] implies that the normal velocity is proportional to the gradient, or Nr^{N-1}. Comparing this term at the crystal surface and assuming an identical radius R for $N=2$ with $N=3$, one has the ratio of $2/3 \approx 0.67$. This heuristic examination suggests that the tip velocity in 2D should be about 0.67 times that of a 3D system, which is higher than the ratio found for type P sidebranches ($\langle \bar{m}_{sb} \rangle_P \approx 0.54$) and

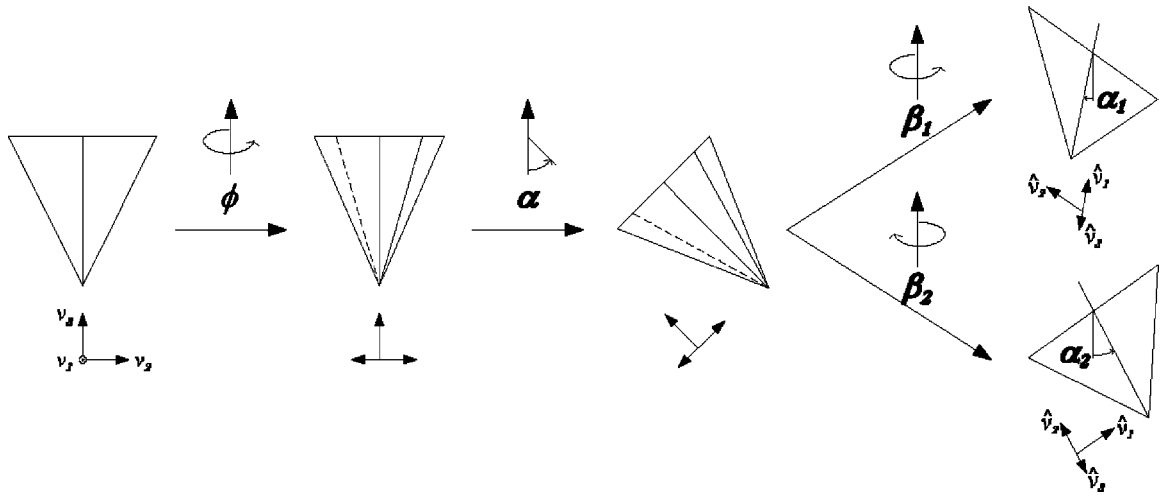

FIG. 21. Orientation of a three-dimensional dendrite. Starting from a dendrite oriented in the observer's coordinate system we apply three rotations: ϕ around the vertical axis (z axis), α around the observation direction (y axis) and again β around the z axis. The angle β can be chosen by turning the capillary. In our experiments β is chosen such as that one symmetry plane is normal to the image plane and the other one appears with a maximum projection area. This leads to the conditions $\beta_3=\beta_1+180°$ and $\beta_4=\beta_2+180°$.

for all sidebranches ($\langle \bar{m}_{\mathrm{sb}} \rangle_{\mathrm{all}} \approx 0.47$). In Refs. [27,28] Altundas and Caginalp studied the growth of succinonitrile dendrite in two and three dimensions using a phase field model. For the velocity of the main dendrite tip a ratio of the 2D to the 3D system was found to be 0.53, which is close to our observations.

ACKNOWLEDGMENTS

Our gratitude goes to our colleagues and collaborators. We thank Dr. H.R. Ott for his support. This work was supported by the Swiss National Science Foundation.

APPENDIX: CONTOUR BACK TRANSFORMATION

We start with a crystal described by the vectors $\{v_1,v_2,v_3\}$, where v_3 corresponds to the growth direction of the main tip and v_1 and v_2 to the growth direction of the sidebranches (see Fig. 21). The vectors are parallel to the observer's coordinate system given by $\{e_1,e_2,e_3\}$, where e_3 is parallel to the direction of the capillary, $-e_1$ is parallel to the direction of observation and the plane spanned by e_2 and e_3 is parallel to the optical object plane.

By successively applying the three rotational matrices

$$R_\phi = \begin{bmatrix} \cos\phi & -\sin\phi & 0 \\ \sin\phi & \cos\phi & 0 \\ 0 & 0 & 1 \end{bmatrix}, \quad R_\alpha = \begin{bmatrix} 1 & 0 & 0 \\ 0 & \cos\alpha & -\sin\alpha \\ 0 & \sin\alpha & \cos\alpha \end{bmatrix}$$

$$\text{and } R_\beta = \begin{bmatrix} \cos\beta & -\sin\beta & 0 \\ \sin\beta & \cos\beta & 0 \\ 0 & 0 & 1 \end{bmatrix},$$

the crystal is oriented in space,

$$\{\hat{v}_1,\hat{v}_2,\hat{v}_3\} = R_\beta R_\alpha R_\phi \{v_1,v_2,v_3\},$$

where R_ϕ, R_α, and R_β are rotations of ϕ, α, and β around e_3, e_1, and e_3, respectively.

A projection matrix

$$P = \begin{bmatrix} 0 & 1 & 0 \\ 0 & 0 & 1 \end{bmatrix}$$

is applied to project the oriented crystal onto the image plane (see Fig. 22),

$$\{\bar{v}_1,\bar{v}_2,\bar{v}_3\} = P\{\hat{v}_1,\hat{v}_2,\hat{v}_3\}.$$

The combination of these transformations can be written as $M=PR_\beta R_\alpha R_\phi$. The whole transformation is described by

$$\{\bar{v}_1,\bar{v}_2,\bar{v}_3\} = M\{v_1,v_2,v_3\},$$

which leads to the projected vectors

$$\bar{v}_1 = \begin{pmatrix} \sin\beta\cos\phi + \cos\alpha\cos\beta\sin\phi \\ \sin\alpha\sin\phi \end{pmatrix},$$

$$\bar{v}_2 = \begin{pmatrix} -\sin\beta\sin\phi + \cos\alpha\cos\beta\cos\phi \\ \sin\alpha\cos\phi \end{pmatrix},$$

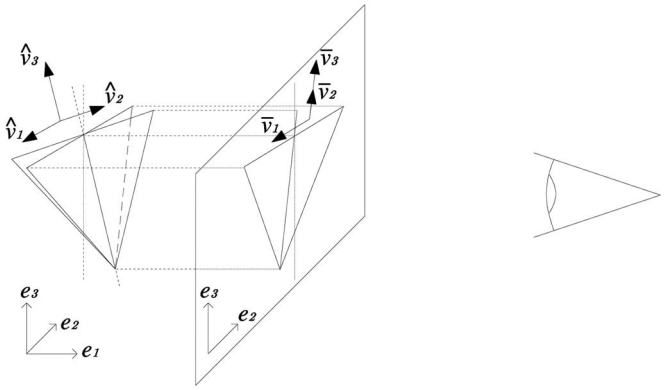

FIG. 22. Projection of a dendrite to the image plane.

$$\bar{v}_3 = \begin{pmatrix} -\sin\alpha\cos\beta \\ \cos\alpha \end{pmatrix}.$$

The condition of one symmetry plane being orthogonal to the image plane is identical to the condition $\bar{v}_1 \| \bar{v}_3$ or $\bar{v}_2 \| \bar{v}_3$ (see Fig. 21). Mathematically these conditions can be written as $\bar{v}_{11}/\bar{v}_{12} = \bar{v}_{31}/\bar{v}_{32}$ and $\bar{v}_{21}/\bar{v}_{22} = \bar{v}_{31}/\bar{v}_{32}$, respectively. This condition is satisfied for four different angles β, where $\beta_3 = \beta_1 + 180°$ and $\beta_4 = \beta_2 + 180°$. It follows

$$\tan\beta_1 = -\frac{\tan\phi}{\cos\alpha}, \tag{A1}$$

$$\tan\beta_2 = \frac{1}{\cos\alpha\tan\phi}. \tag{A2}$$

Resolving Eqs. (A1) and (A2) to $\tan\phi$ and setting them equal leads to

$$\cos^2\alpha = \frac{-1}{\tan\beta_1\tan\beta_2}. \tag{A3}$$

The corresponding angles α_1 and α_2 for the two cases (β_1 and β_2) are defined as the angles between the vertical axis and the projected vector $\bar{v}_3$. This leads to the relations

$$\tan\alpha_1 = \frac{-\bar{v}_{31}}{\bar{v}_{32}} = \frac{\sin\alpha\cos\beta_1}{\cos\alpha}$$

and

$$\tan\alpha_2 = \frac{-\bar{v}_{31}}{\bar{v}_{32}} = \frac{\sin\alpha\cos\beta_2}{\cos\alpha},$$

which is equal to

$$\tan\alpha_1 = \cos\beta_1\tan\alpha, \tag{A4}$$

$$\tan\alpha_2 = \cos\beta_2\tan\alpha. \tag{A5}$$

Inserting

$$\cos\beta_{1/2} = \sqrt{\frac{1}{1+\tan^2\beta_{1/2}}}$$

into Eqs. (A4) and (A5) and reforming leads to

$$\tan\beta_1 = \pm\sqrt{\frac{\tan^2\alpha}{\tan^2\alpha_1} - 1}, \tag{A6}$$

$$\tan\beta_2 = \pm\sqrt{\frac{\tan^2\alpha}{\tan^2\alpha_2} - 1}. \tag{A7}$$

Inserting Eqs. (A6) and (A7) into Eq. (A3) leads to an implicit equation including only α, α_1, and α_2,

$$\cos^2\alpha \times \sqrt{\left(\frac{\tan^2\alpha}{\tan^2\alpha_1} - 1\right)\left(\frac{\tan^2\alpha}{\tan^2\alpha_2} - 1\right)} + 1 = 0.$$

This is a quadratic equation with $x = \cos^2\alpha$ that can be written as

$$Ax^2 + Bx + C = 0,$$

with

$$A = (a+1)(b+1),$$

$$B = [a(b+1) + (a+1)b],$$

$$C = ab - 1,$$

and where

$$a = \frac{1}{\tan^2\alpha_1} \quad \text{and} \quad b = \frac{1}{\tan^2\alpha_2}.$$

The solution is

$$\alpha = \alpha(\alpha_1, \alpha_2) = \arccos\sqrt{\frac{-B - \sqrt{B^2 - 4AC}}{2A}}. \tag{A8}$$

Identifying Eq. (A1) with Eq. (A6) leads to

$$\phi = \arctan\sqrt{\frac{\tan^2\alpha}{\tan^2\alpha_1} - 1}. \tag{A9}$$

For a unique identification of β_1 and β_2 we assume ϕ, α, β_1, and β_2 to be positive.

From Eqs. (A1) and (A2) β_1 and β_2 can still have two different values,

$$\beta_1 = \begin{cases} \arctan\left(-\dfrac{\tan\phi}{\cos\alpha}\right) + \pi, \\ \arctan\left(-\dfrac{\tan\phi}{\cos\alpha}\right) + 2\pi, \end{cases}$$

$$\beta_2 = \begin{cases} \arctan\left(\dfrac{1}{\cos\alpha\tan\phi}\right), \\ \arctan\left(\dfrac{1}{\cos\alpha\tan\phi}\right) + \pi. \end{cases}$$

Reforming Eqs. (A4) and (A5) leads to

$$\beta_1 = \begin{cases} \arccos\left(\dfrac{\tan\alpha_1}{\tan\alpha}\right), \\ 2\pi - \arccos\left(\dfrac{\tan\alpha_1}{\tan\alpha}\right), \end{cases}$$

$$\beta_2 = \begin{cases} \arccos\left(\dfrac{\tan\alpha_2}{\tan\alpha}\right), \\ 2\pi - \arccos\left(\dfrac{\tan\alpha_2}{\tan\alpha}\right). \end{cases}$$

Comparing the intervals of the solutions of the above equations leads to

$$\beta_1 = \begin{cases} \arctan\left(-\frac{\tan\phi}{\cos\alpha}\right) + \pi | \alpha_1 < 0\,^\circ, \\ \arctan\left(-\frac{\tan\phi}{\cos\alpha}\right) + 2\pi | \alpha_1 > 0\,^\circ, \end{cases} \tag{A10}$$

$$\beta_2 = \begin{cases} \arctan\left(\frac{1}{\cos\alpha\tan\phi}\right) | \alpha_2 > 0\,^\circ, \\ \arctan\left(\frac{1}{\cos\alpha\tan\phi}\right) + \pi | \alpha_2 < 0\,^\circ, \end{cases} \tag{A11}$$

depending on the signs of α_1 and α_2.

Using Eqs. (A8)–(A10), the angles α, ϕ, and $\beta=\beta_1$ can be calculated from the two angles α_1 and α_2.

The matrix $\bar{M}$ used for transforming $\{v_2, v_3\}$ to $\{\overline{v_2}, \overline{v_3}\}$ is

$$\bar{M} = \begin{bmatrix} -\sin\beta\sin\phi + \cos\alpha\cos\beta\cos\phi & -\sin\alpha\cos\beta \\ \sin\alpha\cos\phi & \cos\alpha \end{bmatrix}.$$

In the special case of $\beta=\beta_1$ described above (one symmetry plane normal to the image plane) the inverse matrix $T=\bar{M}^{-1}$ is

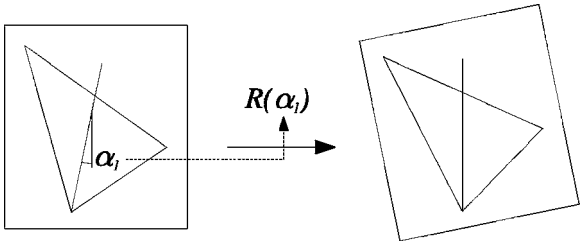

FIG. 23. If only the first angle α_1 is known, only a rotation is applied to orientate the contours parallel to the coordinate system.

$$T = \frac{1}{D}\begin{bmatrix} -\cos\alpha & -\sin\alpha\cos\beta \\ \sin\alpha\cos\phi & \sin\beta\sin\phi - \cos\alpha\cos\beta\cos\phi \end{bmatrix}$$

with $D=\det\bar{M}=\cos\alpha\sin\beta\sin\phi-\cos\beta\cos\phi$. T maps $\overline{v_2}$ and $\overline{v_3}$ to $\overline{e_2}$ and $\overline{e_3}$, respectively. This is the matrix that transforms back the projected crystal to its original proportions,

$$\{v_2, v_3\} = T\{\overline{v_2}, \overline{v_3}\}.$$

As shown schematically in Fig. 23 a back transformation is limited to a simple rotation if only the angle α_1 is known.

[1] J. C. LaCombe, M. B. Koss, D. C. Corrigan, A. O. Lupulescu, L. A. Tennenhouse, and M. E. Glicksman, J. Cryst. Growth **206**, 331 (1999).
[2] C. Giummarra, J. C. LaCombe, M. B. Koss, J. E. Frei, A. O. Lupulescu, and M. E. Glicksman, J. Cryst. Growth **274**, 317 (2005).
[3] D. P. Corrigan, M. B. Koss, J. C. LaCombe, K. D. de Jager, L. A. Tennenhouse, and M. E. Glicksman, Phys. Rev. E **60**, 7217 (1999).
[4] D. P. Woodruff, *The Solid-Liquid Interface* (Cambridge University Press, London, 1973).
[5] E. Hürlimann, R. Trittibach, U. Bisang, and J. H. Bilgram, Phys. Rev. A **46**, 6579 (1992).
[6] B. Chalmers, *Principles of Solidification* (Wiley, New York, 1964).
[7] H. M. Singer and J. H. Bilgram, Phys. Rev. E **69**, 032601 (2004).
[8] Q. Li and C. Beckermann, Acta Mater. **47**, 2345 (1999).
[9] H. M. Singer and J. H. Bilgram, Phys. Rev. E **70**, 031601 (2004).
[10] H. M. Singer and J. H. Bilgram, Physica D **219**, 101 (2006).
[11] U. Bisang and J. H. Bilgram, Phys. Rev. E **54**, 5309 (1996).
[12] U. Bisang and J. H. Bilgram, Phys. Rev. Lett. **75**, 3898 (1995).
[13] E. Brener and D. Temkin, Phys. Rev. E **51**, 351 (1995).
[14] H. M. Singer and J. H. Bilgram, Europhys. Lett. **68**, 240 (2004).
[15] X. W. Qian and H. Z. Cummins, Phys. Rev. Lett. **64**, 3038 (1990).
[16] M. B. Koss, J. C. LaCombe, A. Chait, V. Pines, M. Zlatkowski, M. E. Glicksman, and P. Kar, J. Cryst. Growth **279**, 170 (2005).
[17] L. I. Rubinstein, *The Stefan Problem* (American Mathematical Society, Providence, Rhode Island, 1971).
[18] M. E. Glicksman, R. J. Schaefer, and J. D. Ayers, Metall. Trans. A **7A**, 1747 (1976).
[19] J. H. Bilgram, M. Firmann, and E. Hürlimann, J. Cryst. Growth **96**, 175 (1989).
[20] D. Marr and E. Hildreth, Proc. R. Soc. London, Ser. B **207**, 187 (1980).
[21] H. M. Singer and J. H. Bilgram, J. Cryst. Growth **261**, 122 (2004).
[22] E. Brener, Phys. Rev. Lett. **71**, 3653 (1993).
[23] J. S. Langer, in *Chance and Matter*, edited by J. Souletie, J. Vannimenus, and R. Stora (Elsevier Science, Amsterdam, 1987), pp. 629–711, les Houches, Session XLVI, 1986.
[24] Q. Li and C. Beckermann, Phys. Rev. E **57**, 3176 (1998).
[25] E. Kaufmann, Ph.D. thesis, ETH, Zurich, 2000.
[26] M. Fell, H. M. Singer, and J. H. Bilgram,Mater. Sci. Eng., A **413-414**, 451 (2005).
[27] Y. B. Altundas and G. Caginalp, J. Stat. Phys. **110**, 1055 (2003).
[28] Y. B. Altundas and G. Caginalp, Nonlinear Anal.: Real World Appl. **62**, 467 (2005).